

## Article

# Design and Growth of Low Resistivity P-Type AlGa<sub>N</sub> Superlattice Structure

Yang Liu <sup>1</sup>, Xiaowei Zhou <sup>1,2,\*</sup>, Peixian Li <sup>1,2,\*</sup>, Bo Yang <sup>1</sup> and Zhuang Zhao <sup>1</sup>

<sup>1</sup> School of Advanced Materials and Nanotechnology, Xidian University, Xi'an 710071, China; yliu\_333@stu.xidian.edu.cn (Y.L.); yangbo1@stu.xidian.edu.cn (B.Y.); 22141214314@stu.xidian.edu.cn (Z.Z.)

<sup>2</sup> State Key Discipline Laboratory of Wide Band Gap Semiconductor Technology, Xidian University, Xi'an 710071, China

\* Correspondence: xwzhou@mail.xidian.edu.cn (X.Z.); pxli@mail.xidian.edu.cn (P.L.)

**Abstract:** This work investigated the impact of periodic thickness and doping region on the doping efficiency of the P-type AlGa<sub>N</sub> superlattice. In this paper, the band structure of the simulated superlattice was analyzed. The superlattice structure of Al<sub>0.1</sub>Ga<sub>0.3</sub>N/Al<sub>0.4</sub>Ga<sub>0.6</sub>N, and the AlGa<sub>N</sub> buffer on the sapphire substrate, achieved a resistivity of ~3.3 Ω·cm. The results indicate that barrier doping and low periodic thickness offer significant advantages in introducing a reduction of the resistivity of P-type AlGa<sub>N</sub> superlattice structures.

**Keywords:** superlattice; barrier doping; periodic thickness; low resistivity

## 1. Introduction

Group III nitrides, particularly the Al<sub>x</sub>Ga<sub>1-x</sub>N ternary alloy, exhibit a tunable band gap ranging from 3.4 eV to 6.2 eV with an Al component  $x = 0\sim 1$ , corresponding to the ultraviolet luminescence region with wavelengths ranging from 365 nm to 200 nm [1–3]. AlGa<sub>N</sub>-based electronics have great application prospects, especially in deep ultraviolet light-emitting diodes (DUV-LEDs) [4,5] and solar-blind photodetectors [6,7].

Although UV-LED has made a series of advances [8,9], the realization of P-type doping in AlGa<sub>N</sub> materials as hole injection layers, particularly those with high Al composition such as AlGa<sub>N</sub> and AlN [10,11], for use in the hole injection area has been a global challenge. Since 1989, H. Mano et al. utilized low-energy electron beam irradiation (LEEBI) to process Mg-doped GaN, achieving low-resistance P-type GaN for the first time [12]. Various methods have been explored, including rapid thermal annealing [13,14], polarization-induced doping [15,16], Mg- $\delta$  doping [17,18], and superlattice doping [19,20]. In 2022, Jiaming Wang et al. [18] employed Mg- $\delta$  doping in Al<sub>0.5</sub>Ga<sub>0.5</sub>N, achieving a hole concentration of  $8.1 \times 10^{18} \text{ cm}^{-3}$ . Even though Mg- $\delta$  doping can achieve a higher hole concentration because the metal atoms (Ga and Al) near the surface stop passing through the metal source when Mg- $\delta$  is doped [21], the number of Ga-N bond breaks is greater than that of Al-N bonds at high temperatures because the Ga-N bond energy is less than the Al-N bond energy. A large number of Ga vacancies are left near the doped interface. On the one hand, these vacancies are favorable for Mg atoms to enter the AlGa<sub>N</sub> lattice; on the other hand, a large number of point defects are unfavorable to the crystal quality.

The challenge with Mg-doped AlGa<sub>N</sub> lies in the deepening acceptor position as the Al component increases, leading to an increase in Mg acceptor activation energy, rising from ~170 meV in GaN to ~670 meV in AlN [10]. The elevated activation energy results in only a small fraction of Mg impurities being thermally activated to generate holes at room temperature. This directly leads to a decrease in hole concentration and an increase in resistivity. Additionally, as the Al component increases, the reduction in AlGa<sub>N</sub> lattice constant poses challenges for Mg atom incorporation [22]. Typically, p-GaN is employed as the hole injection layer in the fabrication of DUV devices [23]. Despite the ability to



**Citation:** Liu, Y.; Zhou, X.; Li, P.; Yang, B.; Zhao, Z. Design and Growth of Low Resistivity P-Type AlGa<sub>N</sub> Superlattice Structure. *Micromachines* **2024**, *15*, 596. <https://doi.org/10.3390/mi15050596>

Academic Editor: Goutam Koley

Received: 7 March 2024

Revised: 3 April 2024

Accepted: 25 April 2024

Published: 29 April 2024



**Copyright:** © 2024 by the authors. Licensee MDPI, Basel, Switzerland. This article is an open access article distributed under the terms and conditions of the Creative Commons Attribution (CC BY) license (<https://creativecommons.org/licenses/by/4.0/>).

introduce a very high concentration of holes, GaN itself possesses a band gap of only 3.4 eV, leading to strong absorption of high-energy photons [24]. Researchers often improve the light extraction efficiency by non-polar AlGaIn epilayers [25], inserting distributed Bragg reflectors [26], and photonic crystals [24,27]. Utilizing a p-AlGaIn material with an equivalent band gap as the active region can overcome the issue of GaN light absorption, facilitating structural simplification and reducing subsequent packaging steps.

In this work, the Silvaco TCAD software is employed to simulate the incorporation of Mg acceptors in various regions of the AlGaIn superlattice structure. We investigate the impact of superlattice structure and period number on the P-type doping efficiency of the AlGaIn material. AlGaIn superlattice structures with varying compositions were grown on a sapphire substrate using metal-organic chemical vapor deposition (MOCVD). Additionally, an ultraviolet visible light photometer (UV-VIS) was used to analyze the Al composition of the AlGaIn superlattice. High-resolution X-ray diffraction (HR-XRD) was used to characterize the superlattice structures. A scanning electron microscope (SEM) was used to analyze cross-sections of the superlattice structures. Furthermore, Hall effect tests were used to analyze the resistivity of the AlGaIn superlattice, which can predict the doping efficiency of the superlattice structure.

## 2. Simulation Calculation

In this work, the Silvaco TCAD software (2014 version) was used to simulate the AlGaIn superlattice structures, varying concentrations of P-type doping, superlattice structure, periodicity, and buffer layer design. The structure diagram of the design is shown in Figure 1.

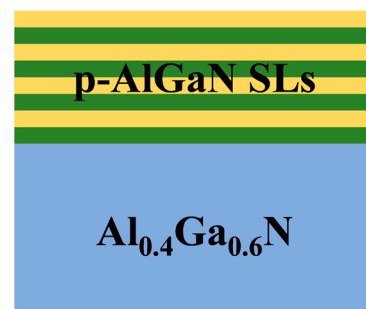


**Figure 1.** Schematic diagram of Silvaco TCAD simulated superlattice structure.

We investigated the factors influencing the P-type doping efficiency of the superlattice. Figure 2 illustrates the theoretically calculated average hole density in the Mg-doped (5 nm/5 nm)  $\text{Al}_{0.1}\text{Ga}_{0.9}\text{N}/\text{Al}_{0.4}\text{Ga}_{0.6}\text{N}$  superlattice structure, grown for 10 cycles on the  $2\ \mu\text{m}$   $\text{Al}_{0.4}\text{Ga}_{0.6}\text{N}$  buffer. The residual carrier concentration in the buffer region is set at  $1 \times 10^{14}\ \text{cm}^{-3}$ .

In Figure 2a, the red dotted line represents the hole density introduced by the Mg acceptor solely at the barrier layer ( $\text{Al}_{0.4}\text{Ga}_{0.6}\text{N}$ ), while the black dotted line depicts the hole density introduced by the Mg acceptor at the potential well layer ( $\text{Al}_{0.1}\text{Ga}_{0.9}\text{N}$ ). The hole density introduced by doping at the barrier layer is notably higher than that at the potential well layer under the same doping concentration. In Figure 2b,c, the barrier region and the well region were doped individually, with a doping density of  $2 \times 10^{18}\ \text{cm}^{-3}$ . Figure 2d illustrates well barrier co-doping with a doping density of  $1 \times 10^{18}\ \text{cm}^{-3}$ . Given that both the trap layer and the barrier layer have widths of 5 nm, the actual total doping concentration in the superlattice region depicted in Figure 2b–d remains consistent at  $1 \times 10^{18}\ \text{cm}^{-3}$ . However, the average hole concentration introduced varies, and were  $9.1 \times 10^{17}\ \text{cm}^{-3}$ ,  $2.2 \times 10^{17}\ \text{cm}^{-3}$ , and  $5.5 \times 10^{17}\ \text{cm}^{-3}$ , respectively. This indicates that the ionization efficiency of the acceptor is significantly influenced by distinct doping regions, with barrier doping demonstrating a pronounced advantage in hole introduction. As shown in Figure 2b–d, the peak position of hole concentration is at the interface between

the potential well and the barrier. The peak concentration of holes in Figure 2b has exceeded the acceptor concentration, indicating that the band structure at the interface strongly affects the acceptor ionization efficiency.

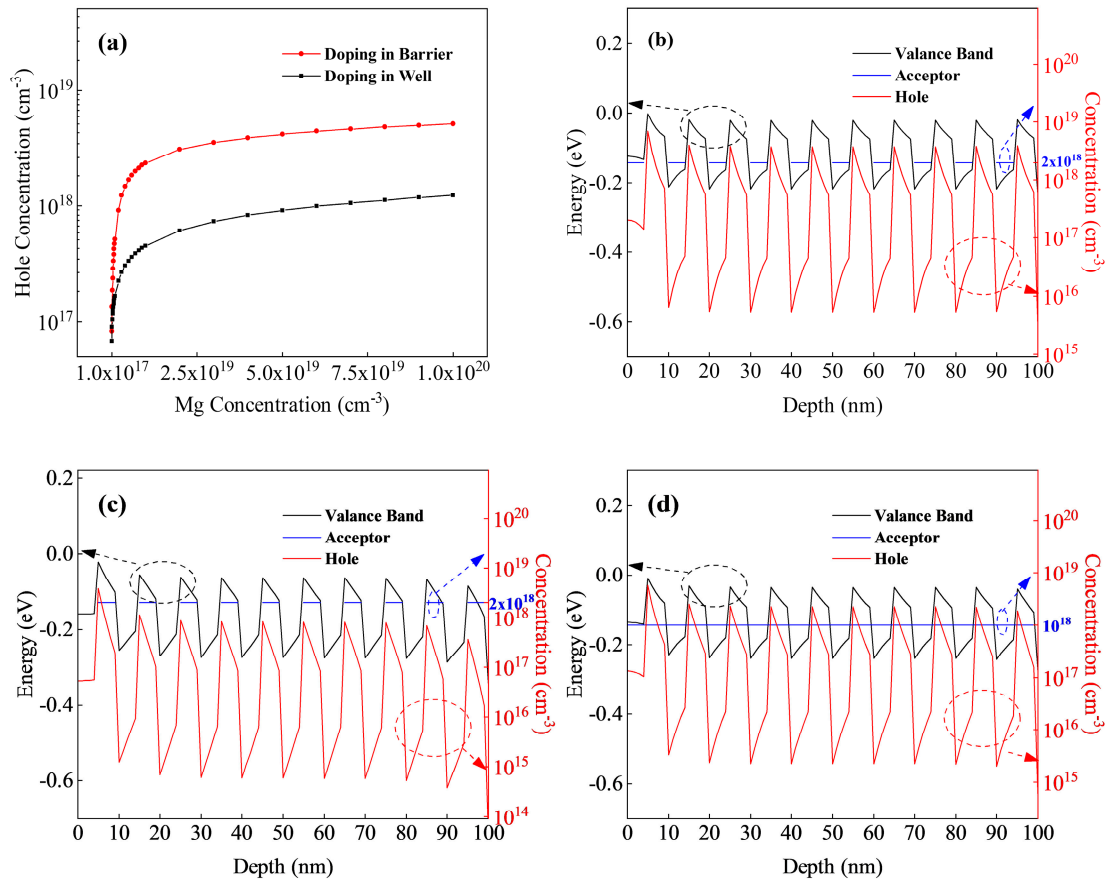


**Figure 2.** Different doping positions and doses: (a) acceptor doping is introduced in different regions of the superlattice structure; (b) barrier region doping, acceptor concentration  $2 \times 10^{18} \text{ cm}^{-3}$ ; (c) potential well region doping, acceptor concentration  $2 \times 10^{18} \text{ cm}^{-3}$ ; (d) well barrier co-doping, acceptor concentrations are  $1 \times 10^{18} \text{ cm}^{-3}$ .

To investigate the impact of superlattice well and barrier Al components on P-type doping, simulation calculations were conducted on a 10-period barrier P-type doped  $\text{Al}_x\text{Ga}_{1-x}\text{N}/\text{Al}_{0.4}\text{Ga}_{0.6}\text{N}$  ( $x = 0.1, 0.2, 0.3$ ) superlattice grown on a  $2 \mu\text{m}$   $\text{Al}_{0.4}\text{Ga}_{0.6}\text{N}$  buffer. The doping concentration is  $2 \times 10^{18} \text{ cm}^{-3}$ , and the trap and barrier each have a thickness of 5 nm, as illustrated in Figure 3.

As shown in Figure 3a, the three groups of  $\text{Al}_x\text{Ga}_{1-x}\text{N}/\text{Al}_{0.4}\text{Ga}_{0.6}\text{N}$  superlattice structures are doped in the barrier region, and the average hole densities are  $9.1 \times 10^{17} \text{ cm}^{-3}$  ( $x = 0.1$ ),  $6.8 \times 10^{17} \text{ cm}^{-3}$  ( $x = 0.2$ ), and  $4.4 \times 10^{17} \text{ cm}^{-3}$  ( $x = 0.3$ ). The acceptor doping concentration is the same, but the hole concentration is significantly different, as shown in Figure 3b. The main energy level of the barrier region is far from the valence band top of the barrier layer, but because of the existence of the superlattice well region, namely the low Al component  $\text{AlGa}\text{N}$ , the barrier region is easily activated by the main energy level, trapping the valence band top electrons in the potential well region and contributing holes, which is conducive to reducing the ionization energy of the acceptance. From Figure 3a, it can be clearly seen that the larger the Al gap between the well region and the barrier region of the  $\text{AlGa}\text{N}$  superlattice is, the larger the valence band top gap is, and the more favorable it is to superlattice P-type doping.

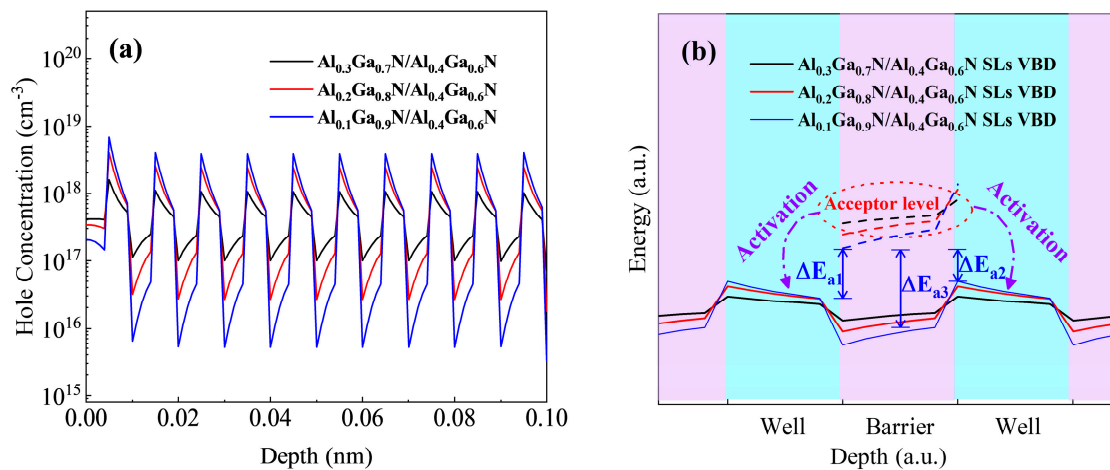


**Figure 3.** Different Al components in the well layer: (a) the change of hole density with location; (b) valence band variation and acceptor activation path.

Additionally, because of the difference in the Al components of the superlattice well and the barrier layer, the average Al component of the superlattice structure changes. Therefore, the superlattice structure of the three groups of samples in Figure 3a is subjected to different stresses in the buffer layer that introduce different piezoelectric polarization electric fields. The  $\text{Al}_{0.1/0.4}$  superlattice structure with the largest difference in Al components between the potential barrier and the potential well is subjected to greater compressive stress in the buffer layer, which is opposite to the direction of spontaneous polarization of the AlGaN material, promoting the formation of a polarization charge and generating more polarization-induced holes. This polarization is reflected in the band diagram in Figure 3b as a sharp change in the slope of the valence band at the junction of the barrier and the well.

In previous studies, the resistance of superlattice structures in the vertical direction was inversely proportional to the thickness of the structure [18,28]. The resistivity is determined by carrier mobility, carrier concentration, and temperature. We designed our experiment to change the period number of the superlattice structure to study the effect of the period number of the superlattice on the P-type doping efficiency of the AlGaN superlattice, and simulated the 10-, 20-, and 40-period superlattice and found that the period number has little effect on the average hole density. This means that the transport efficiency of the holes in the vertical direction varies with the superlattice period, that is, the more cycles there are, the higher the mobility of the holes in the vertical direction. As stated in the resonant tunneling model proposed by R. Tsu and L. Esaki et al. [29], the barrier layer of the superlattice structure is narrow, and the bound energy levels between each quantum well can be coupled to form microstrips. The greater the number of periods, the wider the microstrip width and the smaller the series resistance.

### 3. Experiment

All samples were grown on 2 in sapphire substrates using Metal-Organic Chemical Vapor Deposition (MOCVD) equipment (AIXTRON CRIUS 2, Herzogenrath, Germany), and TMAI, TMGa, and  $\text{NH}_3$  were used as the sources, with  $\text{H}_2$  as the carrier gas. Firstly, the low temperature AlN nucleation layer of 20 nm was grown at 620 °C. Secondly, the temperature of the reaction chamber is raised to 1080 °C to grow 500 nm AlN and 500 nm  $\text{Al}_{0.75}\text{Ga}_{0.25}\text{N}$  as the transition layer. Then, 1.5  $\mu\text{m}$  of AlN buffer is grown by epitaxy. Finally, the superlattice structure is grown. Only superlattice barrier P-type doping was performed, using  $\text{Cp}_2\text{Mg}$  as the dopant with a flux of 280 sccm. The superlattice structure was controlled in 10 cycles. After the epitaxy was completed, each sample was annealed in a  $\text{N}_2$  atmosphere at 850 °C for 10 min and regional information is detailed in Table 1. The only difference among samples A, B, and C lies in the period thicknesses, which were 6 nm,

8 nm, and 10 nm, respectively; the only difference among samples C, D, and E lies in the Al composition of the well layers, which were 0.3, 0.2, and 0.1, respectively. Figure 4a is a schematic diagram of the sample.

**Table 1.** Information on potential wells and barriers of superlattice structures.

Sample		A	B	C	D	E
Well	Al Composition	0.3	0.3	0.3	0.2	0.1
	Thickness (nm)	3	4	5	5	5
Barrier	Al Composition	0.4	0.4	0.4	0.4	0.4
	Thickness (nm)	3	4	5	5	5

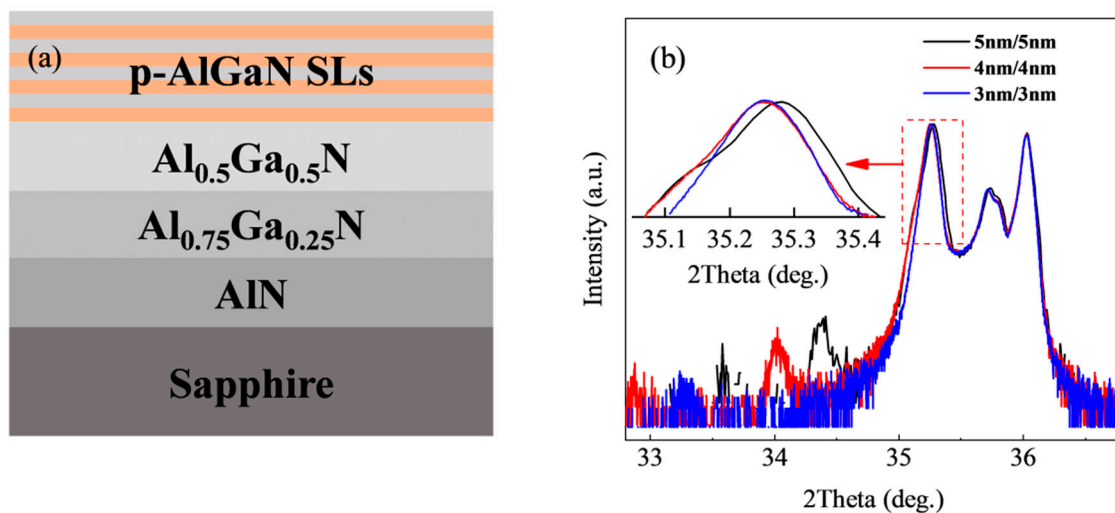


**Figure 4.** (a) Schematic illustration of the sample; (b) HR-XRD diffraction pattern scanned by 2theta-omega on the surface (0002) of the superlattice sample with different period thicknesses, 3 nm/3 nm, 4 nm/4 nm, and 5 nm/5 nm.

Figure 4b shows the superlattice structure with a designed barrier and well thickness of 4 nm, and the diffraction peak and superlattice satellite peak of the buffer layer are clearly visible. The designed superlattice structure has an average Al composition of 0.25, and the superlattice 0-level satellite peak is expected to be near  $35.07^\circ$ . Additionally, the 2theta distance of the superlattice satellite peak near  $32.95^\circ$  and  $34.02^\circ$  is  $1.12^\circ$ , providing evidence for the existence of a superlattice 0-level satellite peak near  $35.1^\circ$ . Since the total thickness of the grown superlattice structure is  $\sim 80$  nm, it is too thin compared with the  $\sim 1.5 \mu\text{m}$  of  $\text{Al}_{0.5}\text{Ga}_{0.5}\text{N}$  buffer, so the 0-level peak signal of the superlattice is weaker and is covered by the signal of the buffer layer.

In order to verify this conjecture, we adjusted the periodic thickness of the superlattice layer, as shown in Figure 4b. The illustration of Figure 4b shows that the 2theta range is  $35.05^\circ$  to  $35.45^\circ$ . It can be seen that on the left side of the Buffer1 peak, the broadening intensifies as the thickness of the superlattice increases, and the superlattice 0-level peak signal becomes stronger. However, there is a broadening on the right side of the Buffer2 diffraction peak in all three samples, and the signal only increases slightly when the superlattice period thickness is 10 nm and the position does not change with the superlattice period thickness. It is speculated that the junction between AlN and  $\text{Al}_{0.75}\text{Ga}_{0.25}\text{N}$  grows on the substrate and Ga atoms and Al atoms diffuse toward each other to form a gradient layer of Al components between 0.75 and 1, which is called Buffer3. This broadening has existed in previous studies but has not been described in detail [30,31].

In order to study the source of the signal change, we grew  $\text{Al}_x\text{Ga}_{1-x}\text{N}/\text{Al}_{0.4}\text{Ga}_{0.6}\text{N}$  superlattice structures with Al components  $x = 0.1$  and  $0.2$  and potential well and barrier thickness of 5 nm on the same buffer structure, as shown in Figure 5.

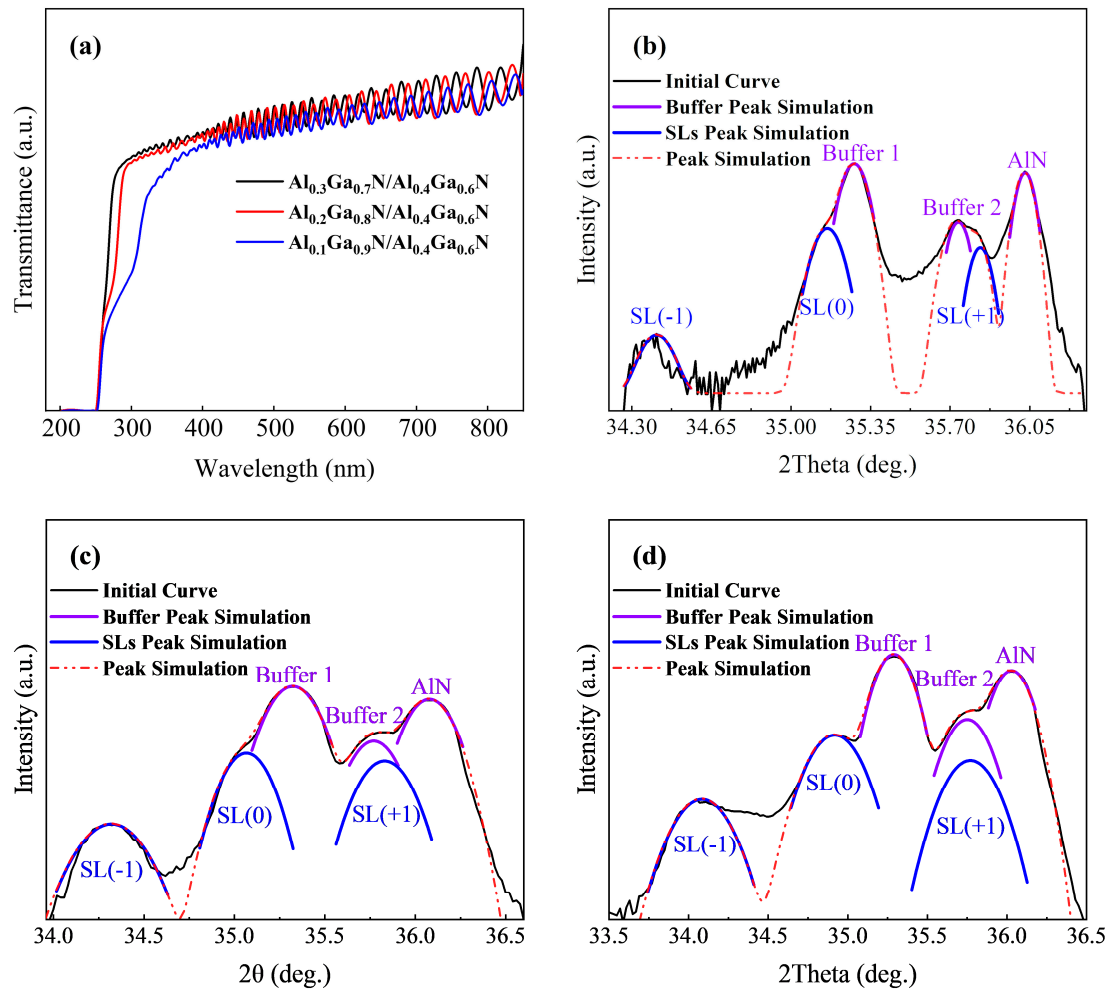


**Figure 5.** (a) UV-VIS transmittance curves of the three groups of samples; (b–d) HR-XRD (0002) 2theta-omega scanning fitting curves of the three samples.

In Figure 5a, the transmittance curves of the three sample groups exhibit significant absorption starting at 280 nm, 290 nm, and 305 nm. The corresponding Al compositions are 0.36, 0.31, and 0.24, closely matching the average Al components of the designed superlattice structure (0.35, 0.31, and 0.24). The thickness of the superlattice region of all samples is  $\sim 100$  nm, and the change of the Al component in the superlattice structure  $\text{Al}_x\text{Ga}_{1-x}\text{N}/\text{Al}_{0.4}\text{Ga}_{0.6}\text{N}$  has little effect on the change of the Al component in the whole sample. However, in the band below 305 nm, all samples have a strong absorption effect, indicating that in order to reduce the light absorption of the DUV-LED p-layer, it is necessary to increase the Al component in P-type region.

The XRD diffraction of the superlattice follows the Bragg equation [32,33]:

$$2D\sin\theta_L = L\lambda, \quad (1)$$

In Equation (1),  $D$  is the periodic thickness of the superlattice structure,  $L$  is the order of the satellite peak in  $2\theta$ - $\omega$  scanning, and  $\theta_L$  is the Bragg angle corresponding to the satellite peak. The superlattice structure has symmetric diffraction. For HR-XRD diffraction

of the superlattice, the corresponding distance  $\Delta\theta$  between two adjacent satellite peaks is expressed by Equation (2):

$$\Delta\theta = \frac{\lambda}{2D\cos\theta} \Delta L \quad (2)$$

In Equation (2),  $\theta$  is the average Bragg angle of the two satellite peaks. Let  $\Delta L = 1$ , then the superlattice structure thickness can be approximated as:

$$D = \frac{\lambda}{2\Delta\theta \cos\theta} \quad (3)$$

According to Equation (3), the scanning pattern of the HR-XRD (0002)  $2\theta$ - $\omega$  superlattice structure in Figure 4 is processed, and the satellite peak position is obtained, as shown in Table 2.

**Table 2.** HR-XRD scanning  $2\theta$  peak information of all samples.

Sample	A	B	C	D	E
SLs(−1)	33.3°	34.02°	34.39°	34.27°	34.08°
SLs(0)	35.09°	35.09°	35.10°	35.01°	34.92°
SLs(+1)	/	/	35.82°	35.78°	35.75°
Buffer 1	35.26°	35.25°	35.27°	35.28°	35.29°
Buffer 2	35.72°	35.74°	35.73°	35.72°	35.75°
AlN	36.03°	36.02°	36.03°	36.03°	36.03°
SLs Al Composition	0.36	0.36	0.37	0.31	0.25
SLs Periodic thickness (nm)	5.2	8.8	12.3	12.5	11.0
Resistivity ( $\Omega$ ·cm)	6.2	23.7	66.2	16.1	3.3

In Figure 5b–d, the positions of the superlattice satellite peaks in the three sample groups shift to the left as the Al component decreases, while the average peak spacing (theta) remains approximately  $0.35^\circ$ . Following peak splitting simulation, depicted in Figure 5b–d, when the Al component of the well layer decreases, the average Al component of the superlattice structure also decreases. This leads to an increase in compressive stress in the superlattice layer, a decrease in the C-axis lattice constant, a reduction in the (0002) crystal plane spacing, and a leftward shift in the satellite peak position of the superlattice. However, since the periodic thickness remains constant, the distance between superlattice satellites also remains constant. Consequently, the position of the superlattice satellite peak SL(+1) in Figure 4b precisely coincides with the signal position caused by Buffer3. In contrast, the superlattice structures with periodic thicknesses of 8 nm and 6 nm in Figure 3 appear relatively small due to their reduced periodic thickness. The position of the SL(+1) peak in the gradient region does not impact its signal due to its specific position. Consequently, the signal at the Buffer3 position in Figure 3b only exhibits a slight elevation in the  $\text{Al}_{0.3}\text{Ga}_{0.4}\text{N}$  superlattice structure with a periodic thickness of 10 nm. All the peak information is shown in Table 2.

The hole concentration in the AlGaIn material can be expressed by the following formula [22]:

$$P = \frac{(N_A - N_D)}{1 + g_p/N_V \exp(\Delta E_A/kT)} \quad (4)$$

In Equation (4),  $N_A$  is the acceptor concentration of AlGaIn,  $N_D$  is the donor concentration,  $g_p$  is the degeneracy factor,  $N_V$  is the valence-capped effective state density, and  $E_A$  is the acceptor activation energy.

As shown in Equation (4), the hole concentration  $P$  is a function of the net acceptor doping concentration ( $N_A - N_D$ ) and the acceptor element activation energy ( $E_A$ ). The relationship between hole concentration and net acceptor doping concentration is linear, while the relationship between hole concentration and acceptor activation energy is a

negative exponential. Therefore, the hole concentration depends mainly on the acceptor activation energy. The activation energy of  $\text{Al}_{0.27}\text{Ga}_{0.73}\text{N}$  was 0.31 eV by Mg doping [34]. At room temperature, the same net acceptor concentration was maintained, the Mg acceptor activation energy  $E_A = 0.31$  eV in  $\text{Al}_{0.27}\text{Ga}_{0.73}\text{N}$  was reduced to  $E_A = 0.17$  eV in GaN, and the hole concentration was increased by  $\sim 1$  order of magnitude. Superlattice structures make this possible. Due to the different bandgap widths of superlattice materials, the energy bands at the interface of the two materials will mutate, and the conduction band and valence band will produce the same periodic oscillation of the superlattice period [35]. The acceptances at the interface between the potential well and the potential barrier will undergo dissociation, and the holes generated by the dissociation will occupy the edge of the valence band far away from the Fermi level, forming a periodic distribution of quasi-two-dimensional hole gas. Although this void gas is not continuous, its average void concentration still exceeds the doping in the bulk material, as shown in Figure 1.

Room temperature Hall effect tests were performed on all samples, and Table 2 illustrates that when the thickness of the superlattice trap and barrier decreases (sample A and sample B), it leads to a decrease in resistivity. This is due to the increase in energy band oscillation amplitude as the periodic thickness decreases. The acceptor energy level of the barrier layer decreases in relation to the valence band top position of the well layer, making the acceptor more easily ionized. This results in a decrease in the acceptor activation energy, promoting an increase in hole density. Consequently, when the periodic thickness of the superlattice is reduced from 12.3 nm to 5.2 nm, the resistivity decreases by approximately one order of magnitude. When the superlattice period thickness remains constant, reducing the Al component of the well layer also contributes to an increase in hole density and a decrease in resistivity. Because of the presence of the low Al component well layer, the deep activation path of the barrier layer becomes shorter, making it easier to be ionized, as depicted in Figure 2b.

In Table 2, the Al component of AlGa<sub>N</sub> buffer structure changes from 1 to 0.5,  $\text{Al}_{0.5}\text{Ga}_{0.5}\text{N}$  of  $\sim 1.5$   $\mu\text{m}$  is grown, and the total thickness of all superlattice structures is  $\sim 100$  nm. The buffer provides compressive stress to the superlattice structure and is responsible for inducing the formation of holes. For samples A, B, and C, the lattice constants between the barrier and the potential well are close to each other, and a slowly changing region is easily formed, which is similar to the growth of a layer of the Al component of the  $\sim 0.35$  AlGa<sub>N</sub> material on the  $\text{Al}_{0.5}\text{Ga}_{0.5}\text{N}$  buffer. On the whole, the compressive stresses are smaller than that of samples D and E, and the hole densities induced by polarization are smaller than that of samples D and E. However, because the periodic thicknesses of samples A and B are small and the valence band changes more steeply, which is conducive to hole transmission, the resistivities of samples A and B are much smaller than that of sample C. However, the Al components in the potential barrier and potential well regions of the superlattice structure of samples D and E differ greatly, and the average Al components are lower. Therefore, the polarization induced holes and the Mg acceptances work together to make samples D and E have higher hole densities. At the same time, the band gaps of samples D and E are very different; the band at the junction of the potential well and the barrier changes, forming a conductive channel near the potential well, and the holes are transported in the form of two-dimensional hole gas, resulting in the low resistivities of samples D and E.

In order to verify the effect of polarization induction and acceptor doping on the AlGa<sub>N</sub> superlattice, we grow an AlGa<sub>N</sub> superlattice sample F with the same structure as sample E on a GaN buffer. The SEM and HR-XRD scanning patterns of its cross-sections are shown in Figure 6.

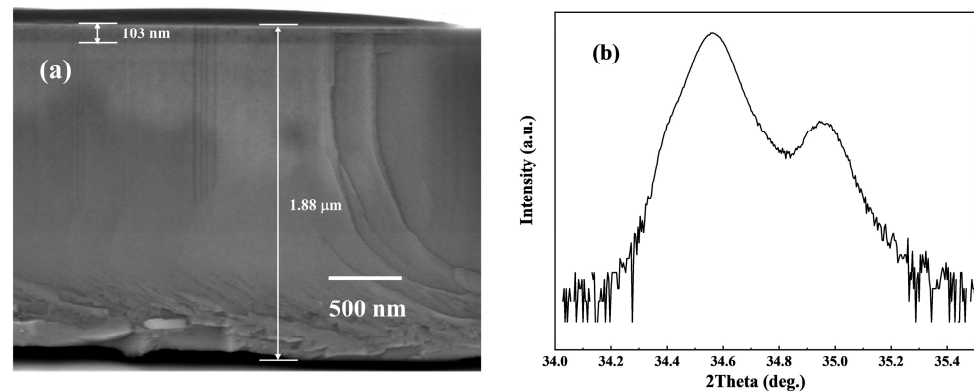


**Figure 6.** (a) Cross-section of growing AlGaIn superlattice on a GaN buffer; (b) HR-XRD (0002) 2theta-omega scanning fitting curves of sample F.

As shown in Figure 6a, the superlattice structure cannot be seen in the SEM scanning image. In Figure 6b, in the HR-XRD  $2\theta$ - $\omega$  scan of sample F, the satellite peak of the superlattice structure cannot be seen. Only the GaN buffer peak around  $34.57^\circ$ , the AlGaIn peak around  $34.95^\circ$ , and some miscellaneous peaks can be seen. As calculated from Equation (1), the component of Al is 0.27. The superlattice structure cannot be seen in the SEM scanning image. This phenomenon is due to the fact that the buffer layer uses a GaN with a large lattice constant to exert tensile stress on the upper AlGaIn structure, resulting in the insufficient periodic transition of the superlattice structure; the small periodic thickness of the superlattice structure is also the main factor.

The hall effect of sample F was tested at room temperature and its resistivity was found to be  $\sim 209 \Omega \cdot \text{cm}$ , which is two orders of magnitude higher than that of sample E. It is about three times higher than the sample C with the highest resistivity on the AlGaIn buffer. Such a high resistivity difference is due to the different types of stress on the superlattice structure caused by different buffer materials. Empirically, we can view the superlattice as the bulk material of strain and the buffer layer as the bulk material of relaxation. Then the superlattice structure is subjected to both piezoelectric polarization and spontaneous polarization, and only spontaneous polarization exists in the buffer layer. The difference of polarization intensity near the interface is the polarization surface charge caused by the change of polarization intensity. As shown in Table 2, we know the average Al component in AlGaIn, and according to the polarization effect formula [36], we calculated the tensile stress generated by the GaN buffer on the upper AlGaIn, and compressive stress by the  $\text{Al}_{0.5}\text{Ga}_{0.5}\text{N}$  buffer on the upper AlGaIn SLs.

All the samples grown on the AlGaIn buffer have Al components smaller than or equal to the buffer layer, which ensures that the superlattice structure is subjected to compressive stress. While compressive stress is conducive to improving the crystal quality of the upper superlattice, it also generates a piezoelectric polarization electric field due to piezoelectric polarization. The piezoelectric polarized electric field changes the band structure of the superlattice and induces polarization-induced holes, which is beneficial to increase the hole concentration of the superlattice structure and reduce the resistivity. In sample F, the buffer layer exerts tensile stress when growing the superlattice structure, which is not conducive to material growth. The polarization-induced electrons produced by AlGaIn under tensile stress will passivate the doped acceptor impurities, which is not conducive to the reduction of resistivity.

#### 4. Discussion

Reducing the thickness of the superlattice barrier layer and increasing the difference of Al components between the superlattice well and the barrier are beneficial to reducing the resistivity. The reason is that reducing the thickness is conducive to increasing the probability of tunneling in the hole band, and increasing the difference of Al components

is conducive to band mutation and reducing the activation energy of the acceptor. Both of these methods are beneficial to reduce the longitudinal resistance of the superlattice structure.

The realization of a low resistivity P-type AlGa<sub>N</sub> superlattice structure is not only beneficial to reduce the light absorption of LED devices and improve the output power, but also has broad prospects for field effect tubes. Using a polarization-induced two-dimensional electron gas at the AlGa<sub>N</sub>/Ga<sub>N</sub> heterojunction interface, HEMT devices have developed rapidly, while complementary P-type transistors have developed more slowly. P-type doping in the AlGa<sub>N</sub> superlattice barrier layer is conducive to increasing the concentration of holes, and the high barrier between the potential well layers is conducive to the transverse transport of holes in the potential well, forming a two-dimensional hole gas transport form. Therefore, it is necessary to reduce the tunneling in the hole zone. We can increase the hole concentration by increasing the thickness of the barrier layer and the difference of Al components between the barrier and the potential well, and thus increase the hole transport in the well as much as possible. This has an obvious promoting effect on the development of AlGa<sub>N</sub>-based field effect transistors.

The stress effect of the buffer layer on the superlattice structure is also an important factor affecting the doping efficiency. Therefore, the selection of higher quality sapphire/AlGa<sub>N</sub> templates or single crystal AlN as substrates is another choice to achieve low resistivity p-AlGa<sub>N</sub> superlattices.

## 5. Conclusions

In this study, Silvaco TCAD is employed to investigate the energy band structure and doping characteristics of p-AlGa<sub>N</sub> superlattices with varying components and periodic thicknesses. The results indicate that different doping regions significantly impact the ionization efficiency of the acceptor, with barrier doping having a greater advantage in introducing holes. The superlattice structure was characterized using HR-XRD and UV-VIS, while the doping properties were assessed through Hall effect tests. Adding Mg to the Al<sub>0.1</sub>Ga<sub>0.4</sub>N/Al<sub>0.4</sub>Ga<sub>0.6</sub>N superlattice barrier with a single period thickness of 10 nm for 10 periods results in a resistivity of ~3.3 Ω·cm. These values align with the theoretical analysis.

**Author Contributions:** Writing—original draft, Y.L.; software, Y.L. and B.Y.; validation, X.Z.; investigation, Z.Z.; supervision, P.L. All authors have read and agreed to the published version of the manuscript.

**Funding:** This research was funded by the National Key R&D Program of China (Grant Nos. 2022YFB3604800).

**Data Availability Statement:** All data that support the findings of this study are included within the article.

**Conflicts of Interest:** The authors declare no conflict of interest.

## References

1. Lee, K.E.; Choi, R.J.; Kang, H.; Shim, J.I.; Ryu, S.-W.; Cho, J.; Lee, J.K. Electrochemical Potentiostatic Activation for the Improvement of 270 Nm AlGa<sub>N</sub>-Based UV-C Light-Emitting Diodes. *Ecs J. Solid State Sci. Technol.* **2022**, *11*, 025007. [[CrossRef](#)]
2. Khan, M.A.; Maeda, N.; Yun, J.; Jo, M.; Yamada, Y.; Hirayama, H. Achieving 9.6% Efficiency in 304 Nm p-AlGa<sub>N</sub> UVB LED via Increasing the Holes Injection and Light Reflectance. *Sci. Rep.* **2022**, *12*, 2591. [[CrossRef](#)] [[PubMed](#)]
3. Khan, M.A.; Maeda, N.; Itokazu, Y.; Jo, M.; Iimura, K.; Hirayama, H. Milliwatt-Power AlGa<sub>N</sub> Deep-UV Light-Emitting Diodes at 254 Nm Emission as a Clean Alternative to Mercury Deep-UV Lamps. *Phys. Status Solidi A-Appl. Mater. Sci.* **2023**, *220*, 2200621. [[CrossRef](#)]
4. Zhang, D.; Chu, C.; Tian, K.; Kou, J.; Bi, W.; Zhang, Y.; Zhang, Z.-H. Improving Hole Injection from P-EBL down to the End of Active Region by Simply Playing with Polarization Effect for AlGa<sub>N</sub> Based DUV Light-Emitting Diodes. *Aip Adv.* **2020**, *10*, 065032. [[CrossRef](#)]
5. Chen, Y.; Che, J.; Chu, C.; Shao, H.; Zhang, Y.; Zhang, Z.-H. Balanced Resistivity in N-AlGa<sub>N</sub> Layer to Increase the Current Uniformity for AlGa<sub>N</sub>-Based DUV LEDs. *IEEE Photonics Technol. Lett.* **2022**, *34*, 1065–1068. [[CrossRef](#)]

6. Kalra, A.; Ul Muazzam, U.; Muralidharan, R.; Raghavan, S.; Nath, D.N. The Road ahead for Ultrawide Bandgap Solar-Blind UV Photodetectors. *J. Appl. Phys.* **2022**, *131*, 150901. [[CrossRef](#)]
7. Li, W.; Wang, Y.; Gu, G.; Ren, F.; Zhou, D.; Xu, W.; Chen, D.; Zhang, R.; Zheng, Y.; Lu, H. Polarization-Assisted AlGa<sub>N</sub> Heterostructure-Based Solar-Blind Ultraviolet MSM Photodetectors with Enhanced Performance. *IEEE Trans. Electron Devices* **2023**, *70*, 3468–3474. [[CrossRef](#)]
8. Sun, H.; Mitra, S.; Subedi, R.C.; Zhang, Y.; Guo, W.; Ye, J.; Shakfa, M.K.; Ng, T.K.; Ooi, B.S.; Roqan, I.S.; et al. Unambiguously Enhanced Ultraviolet Luminescence of AlGa<sub>N</sub> Wavy Quantum Well Structures Grown on Large Misoriented Sapphire Substrate. *Adv. Funct. Mater.* **2019**, *29*, 1905445. [[CrossRef](#)]
9. Yu, H.; Memon, M.H.; Wang, D.; Ren, Z.; Zhang, H.; Huang, C.; Tian, M.; Sun, H.; Long, S. AlGa<sub>N</sub>-Based Deep Ultraviolet Micro-LED Emitting at 275 Nm. *Opt Lett* **2021**, *46*, 3271–3274. [[CrossRef](#)]
10. Nam, K.B.; Nakarmi, M.L.; Li, J.; Lin, J.Y.; Jiang, H.X. Mg Acceptor Level in AlN Probed by Deep Ultraviolet Photoluminescence. *Appl. Phys. Lett.* **2003**, *83*, 878–880. [[CrossRef](#)]
11. Zheng, T.; Lin, W.; Cai, D.; Yang, W.; Jiang, W.; Chen, H.; Li, J.; Li, S.; Kang, J. High Mg Effective Incorporation in Al-Rich Al<sub>x</sub>Ga<sub>1-x</sub>N by Periodic Repetition of Ultimate V/III Ratio Conditions. *Nanoscale Res Lett* **2014**, *9*, 40. [[CrossRef](#)] [[PubMed](#)]
12. Amano, H.; Kito, M.; Hiramatsu, K.; Akasaki, I. P-Type Conduction in Mg-Doped GaN Treated with Low-Energy Electron Beam Irradiation (LEEBI). *Jpn. J. Appl. Phys.* **1989**, *28*, L2112. [[CrossRef](#)]
13. Tanaka, T.; Watanabe, A.; Amano, H.; Kobayashi, Y.; Akasaki, I.; Yamazaki, S.; Koike, M. P-Type Conduction in Mg-Doped GaN and Al<sub>0.08</sub>Ga<sub>0.92</sub>N Grown by Metalorganic Vapor Phase Epitaxy. *Appl. Phys. Lett.* **1994**, *65*, 593–594. [[CrossRef](#)]
14. Wu, Z.; Zhang, X.; Fan, A.; Dai, Q.; Zhao, J.; Chen, S.; Feng, Z.C.; Cui, Y. Enhanced Hole Concentration in Nonpolar A-Plane p-AlGa<sub>N</sub> Film with Multiple-Step Rapid Thermal Annealing Technique. *J. Phys. D-Appl. Phys.* **2018**, *51*, 095101. [[CrossRef](#)]
15. Yan, L.; Zhang, Y.; Han, X.; Deng, G.; Li, P.; Yu, Y.; Chen, L.; Li, X.; Song, J. Polarization-Induced Hole Doping in N-Polar III-Nitride LED Grown by Metalorganic Chemical Vapor Deposition. *Appl. Phys. Lett.* **2018**, *112*, 182104. [[CrossRef](#)]
16. Bagheri, P.; Klump, A.; Washiyama, S.; Breckenridge, M.H.; Kim, J.H.; Guan, Y.; Khachariya, D.; Quinones-Garcia, C.; Sarkar, B.; Rathkanthiwar, S.; et al. Doping and Compensation in Heavily Mg Doped Al-Rich AlGa<sub>N</sub> Films. *Appl. Phys. Lett.* **2022**, *120*, 082102. [[CrossRef](#)]
17. Fan, A.; Zhang, X.; Chen, S.; Li, C.; Lu, L.; Zhuang, Z.; Lyu, J.; Hu, G.; Cui, Y. Effects of V/III Ratio and Cp<sub>2</sub>Mg Flow Rate on Characteristics of Non-Polar Alpha-Plane Mg-Delta-Doped p-AlGa<sub>N</sub> Epi-Layer. *Superlattices Microstruct.* **2020**, *145*, 106632. [[CrossRef](#)]
18. Wang, J.; Wang, M.; Xu, F.; Liu, B.; Lang, J.; Zhang, N.; Kang, X.; Qin, Z.; Yang, X.; Wang, X.; et al. Sub-Nanometer Ultrathin Epitaxy of AlGa<sub>N</sub> and Its Application in Efficient Doping. *Light-Sci. Appl.* **2022**, *11*, 71. [[CrossRef](#)] [[PubMed](#)]
19. Ebata, K.; Nishinaka, J.; Taniyasu, Y.; Kumakura, K. High Hole Concentration in Mg-Doped AlN/AlGa<sub>N</sub> Superlattices with High Al Content. *Jpn. J. Appl. Phys.* **2018**, *57*, 04FH09. [[CrossRef](#)]
20. Gu, W.; Lu, Y.; Liu, Z.; Liao, C.-H.; Yan, J.; Wang, J.; Li, J.; Li, X. Enhanced Hole Concentration in Strain-Compensated BAlN/AlGa<sub>N</sub> Superlattice for Deep Ultraviolet Light-Emitting Diodes. *Micro Nanostruct.* **2022**, *163*, 107128. [[CrossRef](#)]
21. Alvi, P.A. Enhanced Optical Gain Characteristics of InAlN/ $\delta$ -Ga<sub>N</sub>/InAlN Nanoscale-Heterostructure for D-UV Applications. *Superlattices Microstruct.* **2020**, *140*, 106436. [[CrossRef](#)]
22. Suzuki, M.; Nishio, J.; Onomura, M.; Hongo, C. Doping Characteristics and Electrical Properties of Mg-Doped AlGa<sub>N</sub> Grown by Atmospheric-Pressure MOCVD. *J. Cryst. Growth* **1998**, *189–190*, 511–515. [[CrossRef](#)]
23. Wang, S.; Zhang, X.; Guo, H.; Yang, H.; Zhu, M.; Cheng, L.; Zeng, X.; Cui, Y. Enhanced Performance of GaN-Based Light-Emitting Diodes by Using a p-InAlGa<sub>N</sub>/Ga<sub>N</sub> Superlattice as Electron Blocking Layer. *J. Mod. Opt.* **2013**, *60*, 2013–2018. [[CrossRef](#)]
24. Liu, Z.; Yu, X.; Zhang, J.; Liu, X.; Ye, J.; Ren, F.-F.; Wang, Y.; Xu, W.-Z.; Zhou, D.; Zhang, R.; et al. Enhanced Light Output from Deep Ultraviolet Light-Emitting Diodes Enabled by High-Order Modes on a Photonic Crystal Surface. *Opt. Lett.* **2023**, *48*, 247–250. [[CrossRef](#)] [[PubMed](#)]
25. Fan, A.; Zhang, X.; Wang, S.; Li, C.; Chen, S.; Zhuang, Z.; He, J.; Hu, G.; Cui, Y. Study of Electrical and Structural Properties of Non-Polar a-Plane p-AlGa<sub>N</sub> Epi-Layers with Various Al Compositions. *J. Alloys Compd.* **2021**, *867*, 159086. [[CrossRef](#)]
26. Cao, D.; Xiao, H.; Yang, X.; Ma, X. Preparation and Improved Photoelectrochemical Properties of InGa<sub>N</sub>/Ga<sub>N</sub> Photoanode with Mesoporous Ga<sub>N</sub> Distributed Bragg Reflectors. *J. Alloys Compd.* **2020**, *853*, 157201. [[CrossRef](#)]
27. Yun, J.; Kashima, Y.; Hirayama, H. Reflectance of a Reflective Photonic Crystal P-Contact Layer for Improving the Light-Extraction Efficiency of AlGa<sub>N</sub>-Based Deep-Ultraviolet Light-Emitting Diodes. *Aip Adv.* **2018**, *8*, 125126. [[CrossRef](#)]
28. Zhao, Y.; Xu, S.; Tao, H.; Zhang, Y.; Zhang, C.; Feng, L.; Peng, R.; Fan, X.; Du, J.; Zhang, J.; et al. Enhanced P-Type Ga<sub>N</sub> Conductivity by Mg Delta Doped AlGa<sub>N</sub>/Ga<sub>N</sub> Superlattice Structure. *Materials* **2020**, *14*, 144. [[CrossRef](#)]
29. Tsu, R.; Esaki, L. Tunneling in a Finite Superlattice. *Appl. Phys. Lett.* **1973**, *22*, 562–564. [[CrossRef](#)]
30. Zhang, J.P.; Wang, H.M.; Gaevski, M.E.; Chen, C.Q.; Fareed, Q.; Yang, J.W.; Simin, G.; Khan, M.A. Crack-Free Thick AlGa<sub>N</sub> Grown on Sapphire Using AlN/AlGa<sub>N</sub> Superlattices for Strain Management. *Appl. Phys. Lett.* **2002**, *80*, 3542–3544. [[CrossRef](#)]
31. Liubchenko, O.; Sabov, T.; Kladko, V.; Melnik, V.; Yukhymchuk, V.; Romanyuk, B.; Kolomys, O.; Hreshchuk, O.; Dubikovskiy, O.; Maksimenko, Z.; et al. Modification of Elastic Deformations and Analysis of Structural and Optical Changes in Ar<sup>+</sup>-Implanted AlN/Ga<sub>N</sub> Superlattices. *Appl. Nanosci.* **2020**, *10*, 2479–2487. [[CrossRef](#)]
32. Sugawara, M.; Kondo, M.; Yamazaki, S.; Nakajima, K. Exact Determination of Superlattice Structures by Small-Angle x-Ray Diffraction Method. *Appl. Phys. Lett.* **1988**, *52*, 742–744. [[CrossRef](#)]

33. Seredin, P.V.; Sharofidinov, S.S.; Goloshchapov, D.L.; Peshkov, Y.A.; Ivkov, S.A.; Buylov, N.S.; Ereemeev, K.A.; Kukushkin, S.A. Nanoscale Raman Mapping of Elastic Stresses in Multilayer Heterostructure Based on Multi-Period GaN/AlN Superlattices Grown Using HVPE Technology on Hybrid SiC/Si Substrate. *Opt. Mater.* **2024**, *150*, 115184. [[CrossRef](#)]
34. Kobayashi, S.; Nonomura, S.; Ushikoshi, K.; Abe, K.; Nishio, M.; Furukawa, H.; Gotoh, T.; Nitta, S. Optical and Electrical Properties of Nano-Crystalline GaN Thin Films and Their Application for Thin-Film Transistor. *J. Cryst. Growth* **1998**, *189*, 749–752. [[CrossRef](#)]
35. Nikishin, S.A.; Borisov, B.; Mansurov, V.; Pandikunta, M.; Chary, I.; Rajanna, G.; Bernussi, A.; Kudriavtsev, Y.; Asomoza, R.; Bulashevich, K.; et al. Short Period P-Type AlN/AlGaIn Superlattices for Deep UV Light Emitters. *MRS Proc.* **2009**, *1202*, 103. [[CrossRef](#)]
36. Ambacher, O.; Majewski, J.; Miskys, C.; Link, A.; Hermann, M.; Eickhoff, M.; Stutzmann, M.; Bernardini, F.; Fiorentini, V.; Tilak, V.; et al. Pyroelectric Properties of Al(In)GaIn/GaN Hetero- and Quantum Well Structures. *J. Phys. Condens. Matter* **2002**, *14*, 3399–3434. [[CrossRef](#)]

**Disclaimer/Publisher’s Note:** The statements, opinions and data contained in all publications are solely those of the individual author(s) and contributor(s) and not of MDPI and/or the editor(s). MDPI and/or the editor(s) disclaim responsibility for any injury to people or property resulting from any ideas, methods, instructions or products referred to in the content.